A MICROSCOPY INVESTIGATION OF RUBBER COMPOUND CRACK PRECURSORS AND TENSILE FRACTURE SURFACES

LEWIS B. TUNNICLIFFE,[1,*] CHRISTOPHER G. ROBERTSON,[2,†] WILLIAM V. MARS[2]

[1]BIRLA CARBON, MARIETTA, GA, USA 30062
[2]ENDURICA LLC, FINDLAY, OH, USA 45840

RUBBER CHEMISTRY AND TECHNOLOGY, Vol. 96, No. 4, pp. 514–529 (2023)

ABSTRACT

Tensile stress–strain testing is used to investigate the fracture behavior of carbon black–reinforced styrene–butadiene rubber, using 50 replicate specimens. Four vulcanized rubber compounds are studied: a CB-filled SBR with standard mixing conditions (control), the same formulation with intentional poor mixing of the CB, and materials identical to the control material but formed by adding minor amounts of 0.5-mm-diameter glass microspheres (beads)—serving as large model defects/inclusions—using a two-roll mill at two levels, corresponding to average values of 0.78 and 6.24 beads per gauge section region of the tensile test specimen. Microscopy analysis of the resulting fracture surfaces was conducted to complement our recent publication on Weibull failure statistics for distributions of tensile strength and crack precursor size. All 200 fractured specimens from tensile testing at 23°C were imaged with light microscopy and exhibited fracture surfaces characterized by relatively smooth planes perpendicular to the uniaxial loading direction. Most tensile failures originated from the edges of the dumbbell specimens, in line with expectations from fracture mechanics. Light microscopy revealed concentric fracture ring features of high specular reflectance emanating from crack precursors, which are a universal feature of the failure process for these compounds and independent of precursor type, size, or location. Noncontact interferometric microscopy confirmed that the rings resulted from variations in surface microroughness, proceeding outward from the precursor as rough–smooth–rough to the edge of the fracture surface. Fracture rings were also observed for tensile tests performed at 80°C. The variation in surface roughness of the fracture surface has parallels to the stick–slip tearing behavior seen for rubbers torn at medium to high rates. To the best of the authors' knowledge, this is the first time that such striking features have been reported. [doi:10.5254/rct-23.201163]

INTRODUCTION

Fracture mechanics approaches can be used to predict the fatigue lifetime of rubber products. The essential inputs are the crack growth rate law and the size of crack precursors.[1–3] This work focuses on the microscopic crack precursors (also referred to as intrinsic flaws or defects) and the morphology of the fracture surface resulting from tensile failure. Crack precursors can arise from undispersed filler agglomerates, regions of high crosslink density arising from incomplete dispersion of curatives, or hard contaminants within the raw materials (e.g., dirt in natural rubber or grit in carbon black), or they can be introduced during rubber processing and from bubbles/voids within the material.[4] Because of their heterogeneous origins, crack precursors are not uniform in size or shape, and the distribution of crack precursor sizes in a rubber material leads to a distribution of failure properties, such as fatigue lifetime and tensile strength. Characterization of crack precursors continues to be an active research area of rubber science.[5–9]

In this article, we continue our previous work on the use of tensile testing to evaluate crack precursor size distributions for various rubber compounds.[10] Tensile failure is the result of two processes:

- Crack nucleation/initiation from precursors within the bulk or at the surface of the rubber compound specimen
- Rapid tearing of rubber from the precursor location to the edges of the specimen

[†]Current affiliation: Polymer Technology Services LLC, Akron, OH, USA 44321

*Corresponding author. email: lewis.tunnicliffe@adityabirla.com

Valuable information can be extracted from tensile testing by considering the fracture mechanics involved in the above processes. Equation 1 gives the tearing energy, T, in a tensile specimen containing a crack precursor (or precrack) of length c, at the edge of the specimen. In Eq. 1, W is the work or strain energy density in the specimen and k is a strain (ε)–dependent parameter defined in Eq. 2. Note that the tearing energy is a function of the strain level and the crack precursor size. If the specimen is strained sufficiently, then the critical tearing energy of the material (T_c) is eventually reached, and catastrophic tearing occurs, starting from the crack precursor. Replacing the parameters in Eqs. 1 and 2 with ultimate properties of the material, we obtain Eq. 3, which is presented in terms of the work (or strain energy density) at break, W_b. Equation 3 provides a direct link between the tensile failure properties of the material, including the elongation (ε_b) and work at break and the crack precursor size (c_0) and critical tearing energy (T_c) of the compound.

$$T = 2kWc \quad [\text{edge crack}] \tag{1}$$

$$k \approx \frac{\pi}{(1+\varepsilon)^{1/2}} \tag{2}$$

$$W_b = \frac{T_c\sqrt{1+\varepsilon_b}}{2\pi c_0} \tag{3}$$

Our previous work[10] demonstrated that Eq. 3 can be used to compute well-resolved precursor size distributions for rubber compounds, provided that a sufficient number of tensile tests are conducted and with additional characterization of T_c for the compounds. In this work, the study is extended to focus on investigations of the resulting tensile failure surfaces. In particular, we focus on where the initiation of fracture is most likely to occur in a tensile specimen and also characterize and interpret the morphology of the resulting fracture surfaces. To achieve this, four different compounds are considered: a carbon black–filled SBR control compound, two compounds identical to the control but containing various loadings of model crack precursors (glass beads), and a carbon black–filled SBR compound with intentionally poor carbon black dispersion quality. Fifty tensile stress–strain to break tests are performed on each compound, and the fracture surfaces are examined using a variety of microscopy techniques.

EXPERIMENTAL DETAILS

MATERIALS, MIXING, AND CURING

Rubber compounds were prepared using a Farrell Banbury 1.5 L internal mixer. The formulations in units of parts per hundred rubber (phr) are given in Table I. The master batch (nonproductive stage) involved mixing for 5 min with mixer cooling water temperature of 40°C using a rotor speed of 77 rpm, which was adjusted as needed during the last 2 min of mixing to reach the drop temperature of 150°C. The final batch (productive stage) involved mixing for 4 min with mixer cooling water temperature of 25°C using a rotor speed of 60 rpm, which was adjusted as needed during the last 2 min of mixing to reach the drop temperature of 100°C. The N550 carbon black material used was an N550 grade having 0 ppm particulate residue recoverable after passing through a 325 mesh screen.[11] N550 was selected because it is one of the most common grades of carbon black used in wide variety of rubber applications. A fine grade of zinc oxide, ZnO 35, was also used with a surface area of 45 m^2/g, which is similar to the N550 carbon black surface area of 40 m^2/g. A compound with poor carbon black dispersion (Poor Dispersion) was created by adding 40% (20 phr) of the carbon black during

TABLE I
RUBBER COMPOUND FORMULATIONS

		Parts per hundred rubber (phr)			
		Control	Poor Dispersion	Bead Low	Bead High
Master batch (nonproductive)	SBR 1500	100	100	100	100
	N550	50	30	50	50
	Zinc oxide	2	2	2	2
	Stearic acid	1	1	1	1
	6PPD A.O.	1	1	1	1
Final batch (productive)	TBBS	2	2	2	2
	Sulfur	2	2	2	2
	N550	—	20	—	—
Two-roll mill	Glass beads ($d = 517$ μm)	—	—	0.09	0.72

the last minute of the productive mixing stage. This procedure was determined via several iterative experiments in order to obtain a suitably poorly dispersed compound. Solid glass beads (microspheres) were purchased from Sigma Aldrich (product ID G8772) and had a density of 2.5 g/cm^3, as reported by the manufacturer. Light-scattering measurements of the microspheres were conducted using a Horiba LA 960 laser diffraction particle size analyzer, which yielded diameters in the range of 452 to 592 μm, with a most probable value of 517 μm (0.517 mm). A two-roll mill was used to add the glass beads to two rubber compounds, one at a lower level of 0.09 phr (Bead Low) and the other at a higher level of 0.72 phr (Bead High). These loading levels correspond, respectively, to volume averages of 0.78 bead and 6.24 beads per gauge section region of the specimen geometry used for tensile testing, and these loadings were confirmed by X-ray computed tomography.[10] The mill gap was 1.5 mm (three times the bead diameter), and the mill temperature was 70°C while the beads were mixed into the rubber. The four rubber compounds were compression molded and cured for 13 min ($\sim T_{90} + 5$ min) at 160°C to form 150 mm × 150 mm × 2 mm thick sheets for testing.

TENSILE TESTING

Test specimens were cut from the 2 mm thick cured rubber sheets in the mill direction using a DIN 53504-S2 dumbbell cutting die, which has a gauge length of 25 mm and a width of 4 mm. The 2 mm thickness is a nominal dimension, and the actual test specimen thicknesses ranged from 2.0 to 2.2 mm, with an average of about 2.1 mm. Simple tension testing of each specimen was performed using an Instron Model 5864 Electro-Mechanical Test Instrument with a 1 kN load cell (2525-806 1 kN; Instron Corp., Norwood, MA, USA). A laser extensometer (model LE-15, full scale 380 mm; Electronic Instrument Research, Irwin, PA, USA) was used for accurate strain measurements. Each specimen was extended at a crosshead travel rate of 4 mm/s until break, and 50 specimens were tested for each compound in order to characterize the failure distribution. The aforementioned tests were all performed at room temperature (23°C). A more limited set of five specimens were tested for the control compound at an elevated temperature of 80°C.

TABLE II
SUMMARY TENSILE STRESS–STRAIN DATA (STANDARD DEVIATION)

	Unit	Control	Poor Dispersion	Bead Low	Bead High
M50	MPa	2.12 (0.05)	2.35 (0.10)	2.09 (0.06)	2.12 (0.07)
M100	MPa	4.68 (0.16)	4.98 (0.28)	4.59 (0.19)	4.73 (0.24)
M200	MPa	12.26 (0.39)	11.54 (0.52)	12.05 (0.51)	12.26[a] (0.54)
M300	MPa	18.92[b] (0.48)	17.38[c] (0.58)	18.57[d] (0.67)	—[e]
Tensile strength	MPa	21.13 (1.12)	18.56 (1.79)	18.87 (2.99)	14.91 (1.85)
Elongation at break	%	341 (24)	323 (34)	308 (54)	239 (29)

[a] Forty-seven specimens of 50 made it past 200% elongation.
[b] Forty-eight specimens of 50 made it past 300% elongation.
[c] Forty specimens of 50 made it past 300% elongation.
[d] Thirty-one specimens of 50 made it past 300% elongation.
[e] Three specimens of 50 made it past 300% elongation.

FRACTURE SURFACE MICROSCOPY

The resulting tensile fracture surfaces were imaged using light optical microscopy (LOM) in reflectance mode using a Nikon SMZ1000 light microscope equipped with a Luminera Infinity 1 camera. To prepare the failure surfaces for microscopy, the surfaces were gently pressed to, and peeled from, scotch tape to remove any accumulated surface dirt. We note that the cleaning of the fracture surfaces in this way did not alter their fundamental appearance, asides from the removal of surface dirt. The predominant source of the dirt was small flecks of silver ink from fiducial markings on the tensile specimens applied for laser extensometer strain measurements. The two surfaces of each tensile failure were then stacked along the mirror axis and imaged. Scanning electron microscopy (SEM) was used to provide a more detailed evaluation of certain fracture surfaces. A ThermoFisher Quattro S ESEM (Waltham, MA, USA) was used in secondary and backscattered modes. No coating of the specimens was required since all compounds were electrically conductive. Interferometric light microscopy (IFM) was used to evaluate the surface micro-roughness of several of the fracture surfaces. A Zygo New View 5000 microscope (Zygo, Middlefield, CT, USA) was used to collect topology images of selected areas of the fracture surfaces measuring 412 μm^2. Postprocessing and analysis of the images was performed in Gwyddion 2.56 freeware software. The surface micro-roughness was characterized by mean surface roughness (R_a) and route mean squared surface roughness (R_q) parameters computed using Gwyddion.

RESULTS

TENSILE STRESS–STRAIN PROPERTIES

Summary stress–strain properties are given in Table II for all 50 tensile test repeats per compound. Values reported are median values. Note that per ASTM D412, the tensile moduli values are reported as the stress at a given elongation percentage; thus, M50 is the tensile stress at 50% elongation, for example. All compounds display similar tensile moduli values; however, the compounds incorporating the glass beads and the compound having poorly dispersed carbon black all exhibit reduced values of tensile strength and elongation at break versus the

well-dispersed control compound. Furthermore, the spread in data for the tensile strength and elongation at break values is indicated by the standard deviations given in parentheses in Table II. As can be seen the "Poor Dispersion," "Bead High," and "Bead Low" compounds, all display much larger spreads in their failure property data than the control material. This has previously been ascribed to differences in size and distributions of crack precursors in these materials.[10]

GENERAL OBSERVATIONS ON FRACTURE SURFACES

Light microscopy images of the failure surfaces of tensile specimens of the four rubber compounds are presented in Figures 1 to 4. A number of observations can be made from these images:

- The fracture surfaces are relatively flat and smooth, with failure having occurred perpendicular to the applied tensile strain. There is little evidence of pronounced roughness or knotty tearing, as would be seen in an NR (strain crystallizing) compound, and the fracture surfaces can be easily focused and imaged within the relatively limited focal plane of the light microscope.
- The overwhelming majority of the failures appear to initiate at or near the edge of the tensile specimens. This is particularly pronounced and obvious for the glass bead–containing specimens.
- Every fracture surface displays a "fracture ring" feature surrounding the initial point of failure. In general, the rubber surface in the immediate vicinity of the initiation point of the failure is darker in appearance, which abruptly transitions to a lighter colored "ring" of high specular reflectance as we move away from the initiation point, which then abruptly transitions back to a darker surface for the remainder of the fracture surface. It is noteworthy that this feature is observed in all compounds of the study, independent of whether the tensile failure originates from, for example, model glass bead precursors or an inherent precursor in the Control or Poor Dispersion compounds. The fracture rings therefore appear to be a universal feature of tensile failure for this compound set and appear independent of crack precursor type, size, and location within the tensile dumbbell. To the best of the authors' knowledge, this feature has not previously been reported in the literature. Several selected LOM images highlighting ring formation for varied combinations of crack precursor type and locations are shown in Figure 5. The fracture ring feature is schematically represented in Figure 6.
- Tensile failures originating from glass beads are very clearly identified in the "Bead Low" and "Bead High" compounds. Dark cavities are observed corresponding to the approximate size of the glass beads (~500 μm). The bright rings observed around the center of these cavities result from refraction of light from the smooth internal surface of the voids. Glass beads are absent from cavities on both fracture surfaces of the tensile failure, being seemingly jettisoned during the failure process. This is illustrated in Figure 7, which shows secondary electron SEM imaging of the Bead High, Specimen 10 fracture surfaces. For the Bead High compound in certain cases (9, 12, 13, 15, 31, 34, 39, 48), the failure originates at a glass bead, and the failure front has evidently encountered another glass bead during propagation. The actual point of failure in such specimens can be identified from the fracture ring phenomena outlined above.

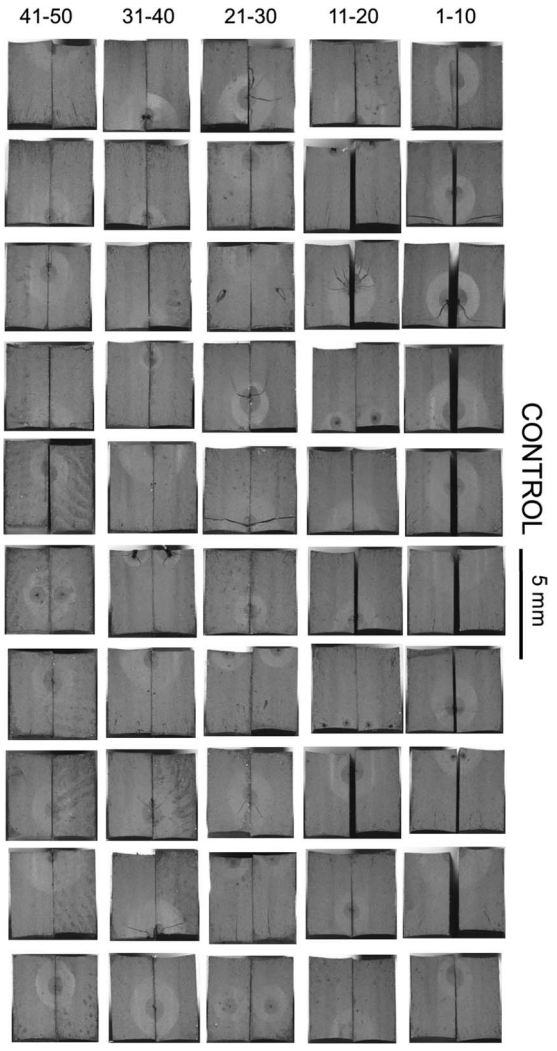

FIG. 1. — Control compound tensile fracture surface micrographs. Each image is an individual tensile specimen, and the two corresponding fracture surfaces are stacked along their mirror axis.

FRACTURE SURFACE FAILURE INITIATION LOCATION

The failure points in each specimen were visually assessed and assigned as either an edge failure or a bulk failure. Table III shows the results of this analysis. For the Control and Poor Dispersion compounds, edge failure was dominant, with roughly 90% of failures originating from a precursor located at or near the edge of the dumbbell. This proportion increased for the glass bead–containing compounds to values of 94% and 100% for the Bead Low and Bead High compounds respectively. The preference for tensile failures originating at the edge of a specimen can be ascribed to the larger tearing energy found for edge versus bulk precracks. This is demonstrated in Figure 8, which shows the results of a finite element analysis simulation of two 10 mm cracks in a block of neo-Hookean rubber with constitutive equation parameters given in the inset to Figure 8. Cracks were located in the bulk of the rubber and at the edge. The rubber was subjected to tensile strains up to 100% tension. Figure 8 (left) shows a snapshot of the

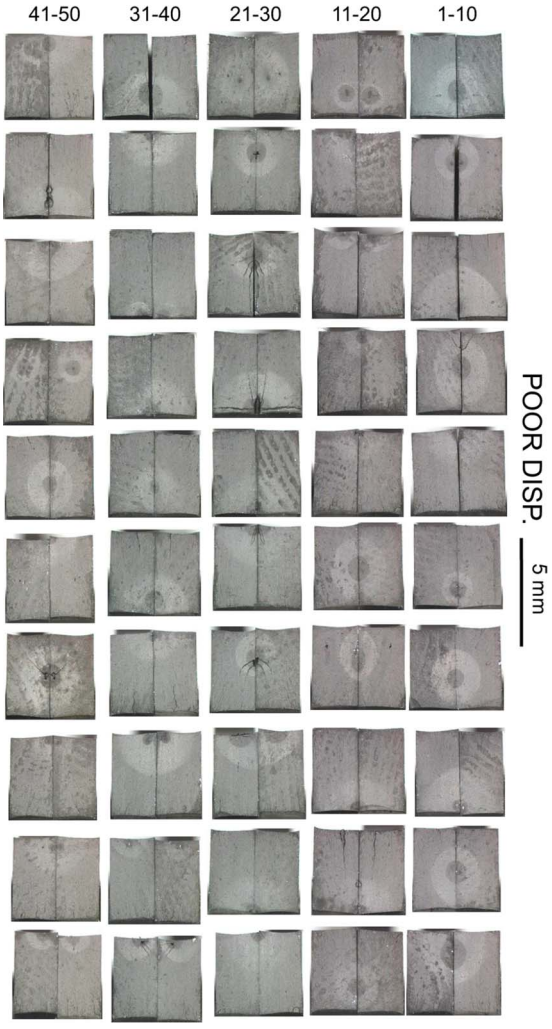

FIG. 2. — Poor dispersion compound tensile fracture surface micrographs. Each image is an individual tensile specimen, and the two corresponding fracture surfaces are stacked along their mirror axis.

simulation at 100% strain. The tearing energy (J integral) associated with each crack was calculated at each strain level, the results of which are shown in Figure 8 (right). A factor of ~2 difference in tearing energy was seen between the edge crack and bulk crack, with the edge crack having twice the tearing energy of the bulk crack. It may be said that the edge crack behaves as if it is twice as large as the bulk crack because the free surface at the edge acts approximately as if it were a plane of mirror symmetry. In practice, this means that in a tensile specimen with two cracks/precursors of equal size, the critical tear energy value, T_c, is reached at lower global strains for the edge precursor, making it the more likely failure point. Therefore, we can contrast Eq. 1, which is derived for an edge precursor/crack, with Eq. 4, which is appropriate for a bulk precursor/crack. This, combined with the existing dependence of tearing energy of a tensile specimen on precursor size, explains both why edge failure is inherently preferred and why increasing precursor size further promotes edge failure occurrence.

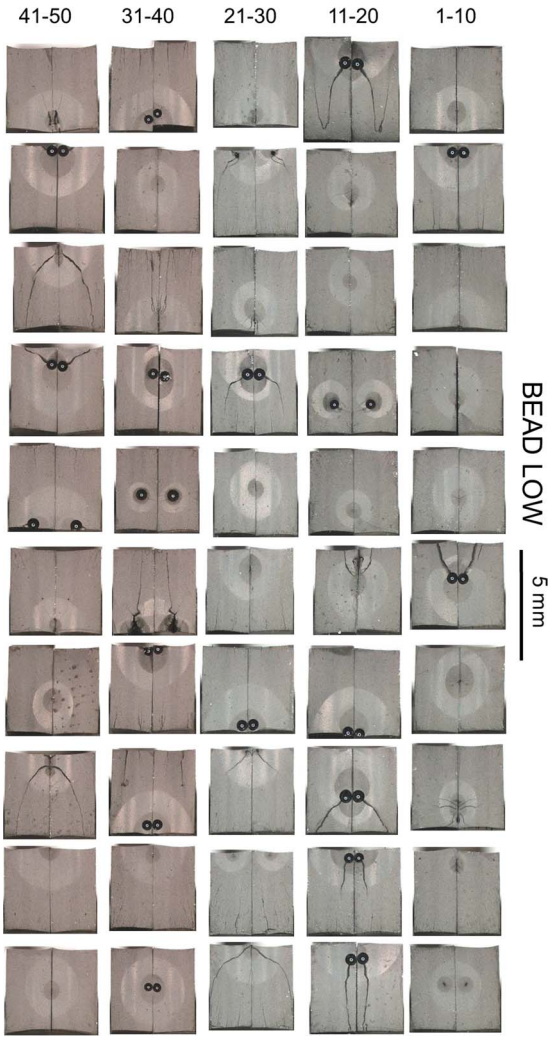

FIG. 3. — Bead Low compound tensile fracture surface micrographs. Each image is an individual tensile specimen, and the two corresponding fracture surfaces are stacked along their mirror axis.

$$T = kWc \quad [\text{internal/bulk crack}] \tag{4}$$

FRACTURE RING SURFACE FEATURES

The fracture ring features were examined using IFM profilometry and SEM. IFM surface topology maps were collected for each of the three zones indicated in Figure 6 on a fracture surface exhibiting a very well-defined fracture ring feature (Control 3). Results of the IFM topological scans are presented in Figure 9, which also overlays the regions in which the various 412 μm^2 scans were collected with the LOM image. As can be seen, the various fracture zones have quite different surface roughness metrics. The roughness metrics presented in Figure 9 are the mean surface roughness (R_a) and the root mean square roughness (R_q) parameters. The fracture ring itself has the lowest mean surface roughness value of $\sim$0.5 μm, which is of the order of the

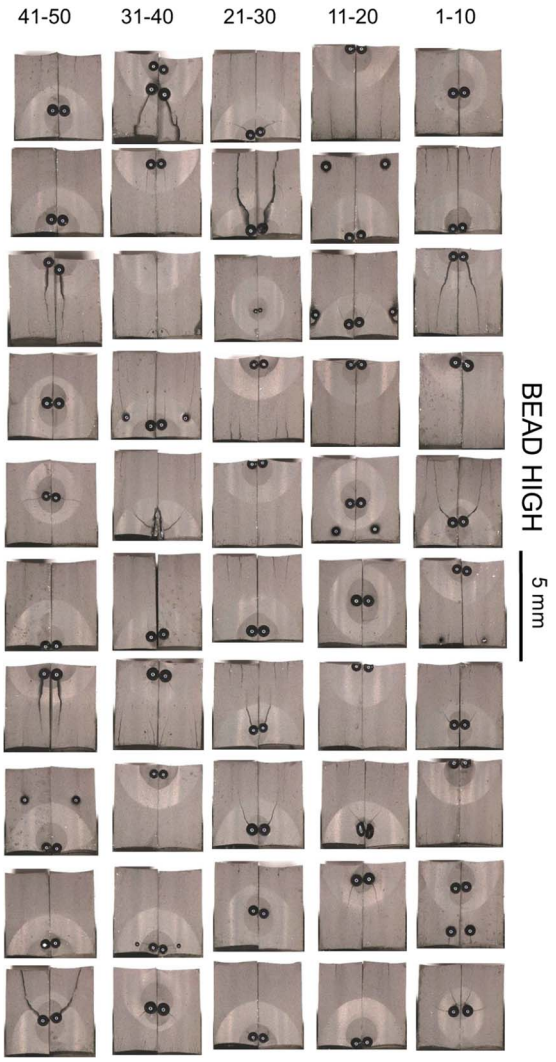

FIG. 4. — Bead High compound tensile fracture surface micrographs. Each image is an individual tensile specimen, and the two corresponding fracture surfaces are stacked along their mirror axis.

wavelength of visible light. The surrounding darker sections of the fracture surface display two to four times higher mean roughness values. The fracture ring feature is therefore a result of contrasting light scattering from tear surface roughness transitions created during fracture. Although the fracture surfaces are in general visually smooth, the fracture ring feature is considerably smoother than the surrounding material to the point at which it appears optically reflective. The same fracture surface (Control 3) was mapped using SEM secondary and backscattered imaging. The stitched composite images are shown in Figure 10. The SEM images confirm the differences in fracture surface topology with clear radial striations being observable in zones 1 and 3 but absent in zone 2 (fracture ring). Figure 10 also shows that the transitions between the various fracture zones and surface roughness are very abrupt.

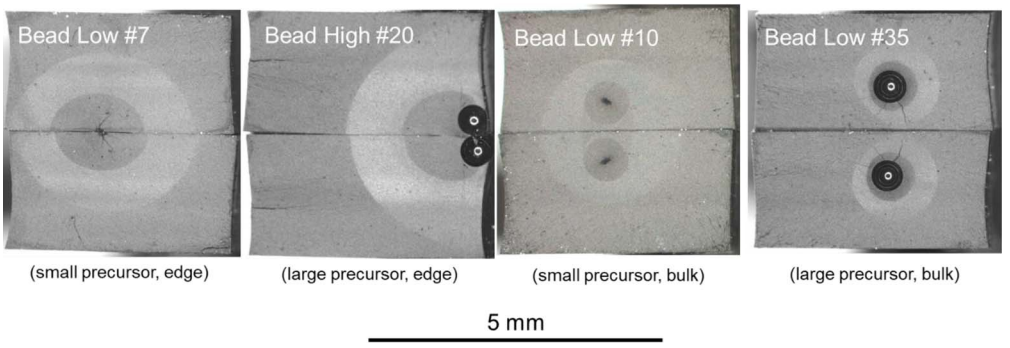

FIG. 5. — Examples of fracture rings from edge and bulk failure initiation and from large (glass bead) and small precursors.

EFFECT OF TENSILE TEST TEMPERATURE

To probe the effect of temperature-dependent viscoelasticity on the fracture rings, a limited number of tensile tests (5×) were performed on the Control compound at 80°C. At this temperature, T_g-related viscoelastic losses in the bulk material and therefore in the region of high strain ahead of the crack tips, are reduced versus room temperature testing. In each tensile failure, the characteristic fracture rings were again observed (Figure 11). Fracture ring features can therefore be observed at different test temperatures.

DISCUSSION

The universal appearance of the fracture ring effect within the sample set for this study is quite remarkable. In fact, following the collection of these results and sensitization to this particular feature, similar fracture rings were observed for a wider range of rubber compounds of differing rubber and filler combinations during routine evaluations at Birla Carbon's rubber laboratory.[12] (Over a period of 4 mo in 2021, fracture rings were observed on the tensile failure surfaces of compounds containing EPDM, NR, and various NR:BR blends, with various carbon blacks ranging in particle size from N700 series to N200 series. In this case, tensile dumbbells were prepared using ASTM 412 Die C geometry. These compounds were selected for examination at random from the workload of Birla Carbon's rubber laboratory.) The tensile test is ubiquitous in the rubber industry, and it is therefore surprising that such a striking feature has not been observed and reported prior to this study. This may be in part due to (1) the large number of specimens tested here (50 dumbbells per compound), which allows us to

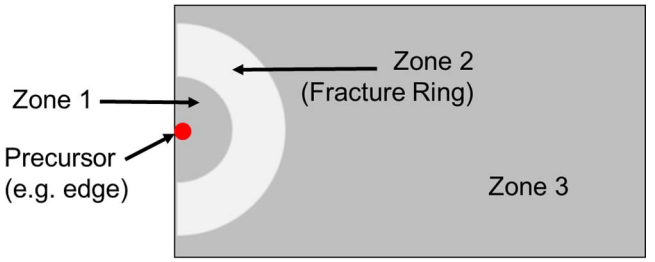

FIG. 6. — Schematic of the fracture ring phenomenon showing a precursor located at the edge of the specimen and the resulting fracture surface divided into three zones.

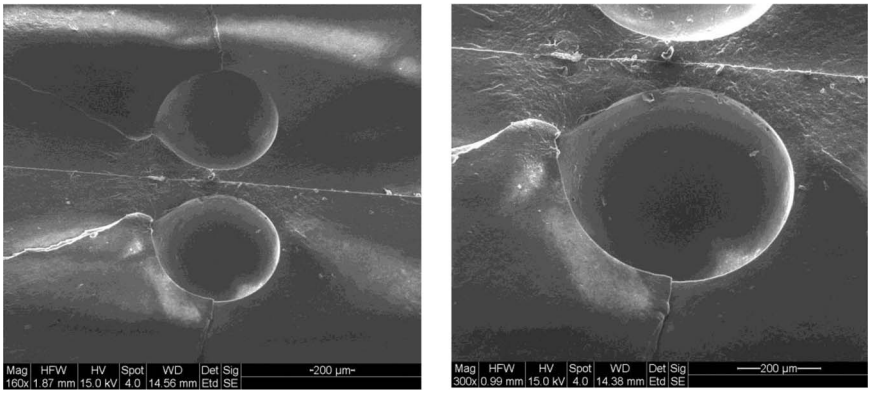

FIG. 7. — Secondary SEM images of cavities in fracture surfaces of specimen Bead High 10, where a glass microsphere has been jettisoned during tensile fracture.

observe the universality of the fracture ring feature; (2) the full-field LOM imaging of both sides of the fracture surfaces, which allows us to observe macroscopic features of the fracture, as opposed to focusing on smaller microscopic or nanoscopic features using higher-resolution techniques such as SEM; and (3) the use of a nonstrain crystallizing rubber (emulsion SBR) as opposed to, for example, natural rubber, for which crack tip deflection as a result of strain crystallite formation ahead of the crack tip during rapid tearing results in a rougher fracture surface, which may somewhat obfuscate observation of fracture rings.

The physical origin of the fracture rings is also worth discussion. While the features reported here for tensile failure surfaces have not been noted or discussed in the literature, a relevant body of work detailing high speed tearing of rubbers is available. Considering that, following initial crack nucleation, tensile failures proceed via a rapid tearing of rubber, there is an obvious parallel between our study and rapid tearing studies. Early work by Greensmith[12] noted the complexity of tear surface roughness of noncrystallizing rubbers as a function of tearing rate and temperature. Kadir and Thomas[13] and later Lake et al.[14] conducted extensive investigations of high-speed tearing of various rubbers. Similar work was also conducted by Tsunoda et al.,[15] who probed the effect of a wide range of rubber compound variables on high-speed tearing. These studies noted that nonstrain crystallizing rubbers undergo transitions in their tear surface morphology as a function of tearing rate. These transitions are summarized schematically in Figure 12, which plots the measured tear energy of the specimens versus the tearing rate. At lower tear propagation rates in region A, the surface of the torn samples is rough. A zone of stick-slip (rough-smooth) tear surface behavior occurs at intermediate tearing rates in region B, after which, at the highest rates of tearing in region C, the tear surface is smooth. Lake et al.[14] commented that the tearing surfaces observed in region C at the highest rates of tearing "are relatively smooth and give good specular reflectance," which is quite consistent with our observations of the fracture rings for the tensile

TABLE III
TENSILE FRACTURE INITIATION LOCATIONS

	Control	Poor Dispersion	Bead Low	Bead High
Edge initiation, No. (%)	45 (90)	45 (90)	47 (94)	50 (100)
Bulk initiation, No. (%)	5 (10)	5 (10)	3 (6)	0 (0)

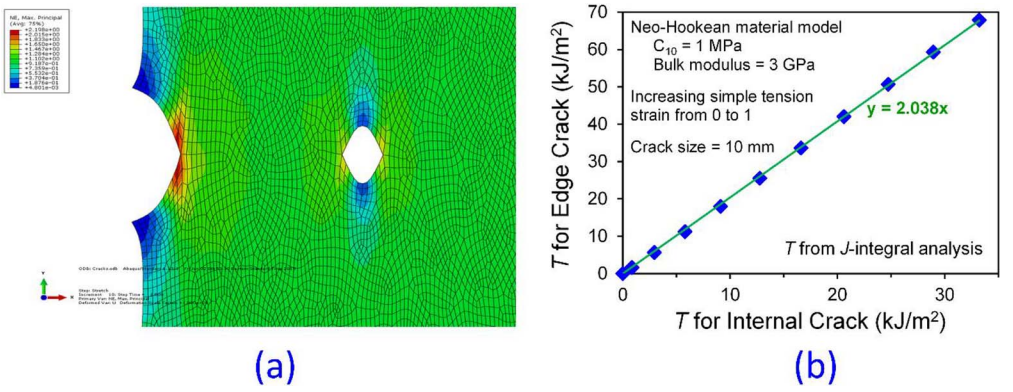

FIG. 8. — Plot (a): Maximum principal strain distribution from Abaqus/Standard 2D finite element analysis for simple tension loading at a strain of 1 (100%) in the vertical direction for neo-Hookean hyperelastic material with indicated material parameters. The geometry has a 10 mm edge crack and a 10 mm internal/bulk crack. Plot (b): T from J-integral analysis for the edge crack versus T for the internal crack for strains from 0 to 1 (symbols) and the linear fit of the results, which yields a slope of 2.038.

fracture surfaces. In the context of Figure 12, it is interesting that the range of T_c values previously determined for our compounds[10] is consistent with the stick-slip tearing region B as determined by Tsunoda et al.[15] for various carbon black–filled SBR compounds.

Lake et al.[14] and Tsunoda et al.[15] proposed that the transitioning in tear surface morphology was due to a suppression of micro-cavitation formation in the process zone ahead of the crack tip at higher tearing rates. They supposed that at lower tearing rates, cavitation occurs in regions of high dilatational stresses ahead of the crack tip, leading to a rougher tear surface. Higher tearing rates induce a viscoelastic stiffening of the rubber in the process zone, which suppresses the formation of these cavities following the well-known relationship describing the onset stresses for cavitation $\sim 5E/6$, where E is the appropriate tensile modulus.[15] In this context, it may be hypothesized that the fracture rings are a manifestation of these tearing instability phenomena and are the result of abrupt acceleration and deceleration in tearing (and therefore changes in tear energy) as the tensile failure proceeds (i.e., slower–faster–slower tearing). The reason for two abrupt changes in tearing rate during tensile failure is unclear at present.

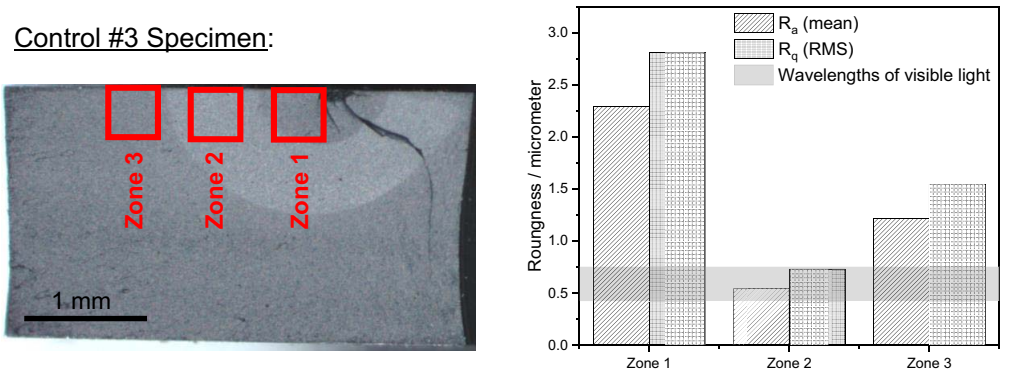

FIG. 9. — IFM surface roughness analysis of the fracture surface of specimen Control 3.

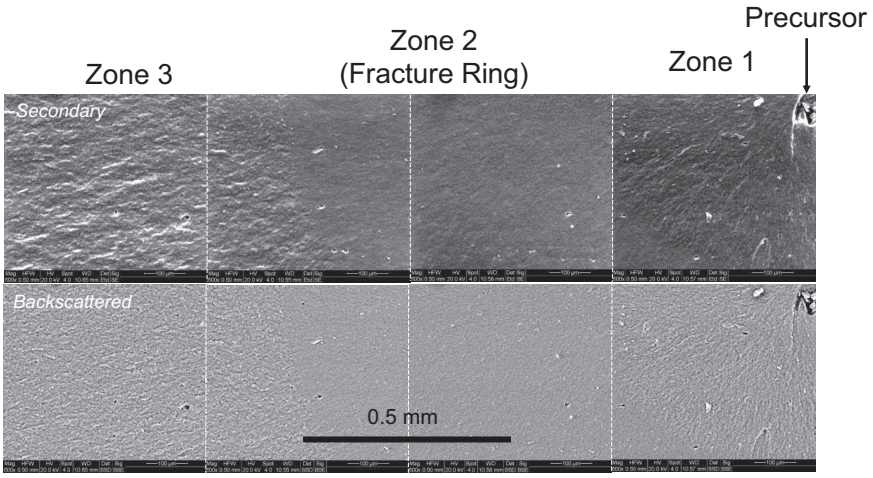

FIG. 10. — SEM secondary (top) and backscattered (bottom) image stitch of a portion of the fracture surface of Control 3.

A second hypothesis for the formation of fracture rings is that the rings result not from tearing initiated at the precursor but from a localized fracture of rubber in the vicinity of the crack precursors prior to failure. In this proposition, rapid fracture would occur first in the smooth ringlike region, near to but at some distance from the precursor, followed by slower tearing outward on both sides of the ring, resulting in overall specimen fracture.

A third hypothesis is that the stress wave traveling through the specimen during rupture results in crack growth rate transients.

In any case, it may be hypothesized that the scale of the roughness of the fracture surface is a reflection of the size of the near crack tip region in which the load on the polymer chains is high enough to cause rupture. Thus, a surface with large roughness corresponds to a process zone in which polymer chains are rupturing in a large volume, and a surface with small roughness corresponds to a more focused process zone where chains break only within a limited volume. This situation is illustrated in Figure 13, where red circles schematically illustrate the relative size/volume of chains undergoing rupture at high strains.

These are topics for further exploration. Further experimental work could include a systematic study of the influence of rubber chemistry, tensile specimen geometry (width, thickness) and testing strain rate as well as studies comparing rapid tear fracture surfaces to tensile failure surfaces.

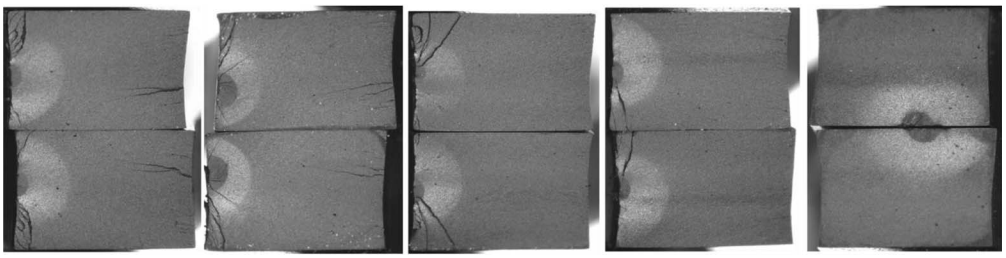

FIG. 11. — Tensile fracture surfaces of the Control compound tested at 80°C.

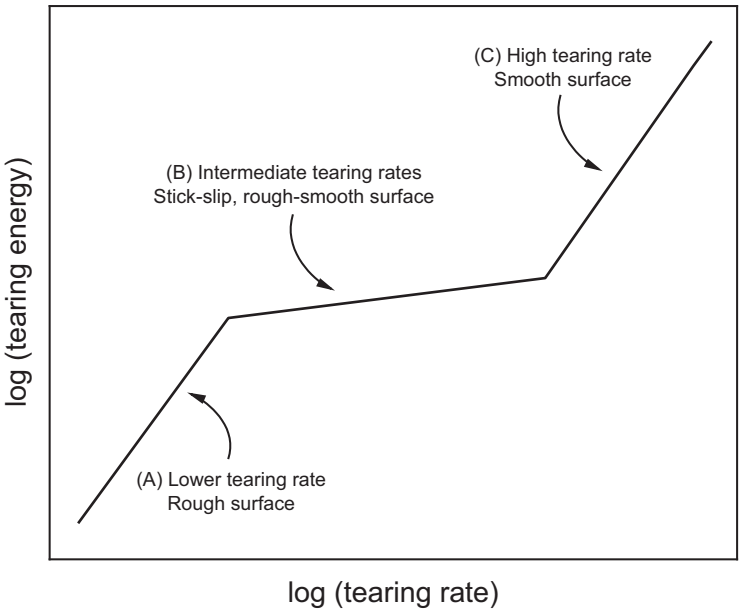

FIG. 12. — Schematic of transitions in the tear behavior of SBR adapted from Tsunoda et al. Tearing energy, T, is plotted as a function of tearing rate, r. Tear surface morphology is indicated on the figure.

CONCLUSIONS

An extensive microscopy analysis of the tensile fracture surfaces of various carbon black–reinforced SBR compounds yielded the following observations and conclusions:

- Tensile failures occur perpendicular to the applied strain and produce relatively flat fracture surfaces.

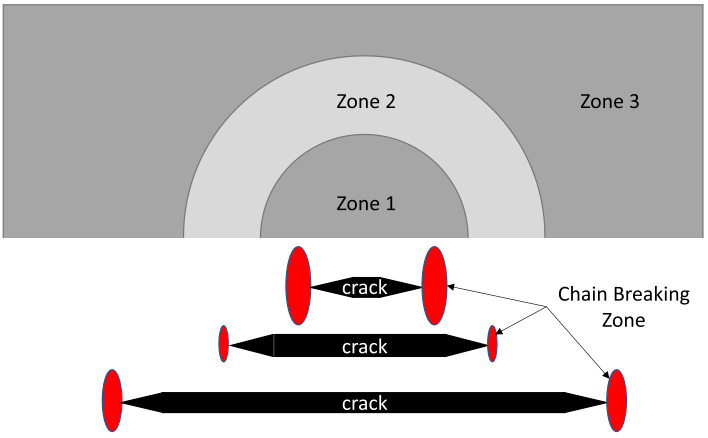

FIG. 13. — Cross-section view of crack during the fracture process, indicating the evolution of chain breaking zone dimensions under the assumption that surface roughness reflects the size of the region where polymer chains are stressed to break.

- Tensile failures are more likely to initiate at the edge of the specimens, and this likelihood is increased when larger precursors are present. This is in line with differences in tearing energies derived for edge versus bulk cracks in tensile specimens.
- Characteristic "fracture rings" are observed for each specimen, independent of precursor type, size, and location as well as tensile test temperature.
- Fracture rings are observable due to contrasts in the scattering of light from regions of pronounced difference in surface roughness across the fracture surface.
- Fracture rings were observed both at room temperature and at elevated temperature.
- Analogies can be drawn between this work and observations on the high-speed tearing of rubber, indicating that the fracture rings may result from an acceleration and deceleration of the crack as it proceeds through the tensile specimen.
- Alternatively, the fracture ring may result from a localized fracture of rubber in the vicinity of the crack precursors just prior to failure or from transient variations of the crack growth rate due to high-speed dynamics of the test specimen.
- The surface roughness may be an indicator of the size of the crack tip zone in which polymer chains are stretched fully to rupture.
- The exact origins of the fracture ring effect require further clarification and present an opportunity for further study.

Finally, we comment that although the tensile test is ubiquitous and has been in use for many decades within the rubber industry, it is still possible to derive new insights into the physical behavior of rubber from such simple tests.

ACKNOWLEDGEMENTS

LBT is deeply indebted to Professor Alan G. Thomas for support and friendship during his time at Queen Mary University of London. The authors thank Mark Bauman for performing the finite element simulation. The authors thank Axel Products, Ann Arbor, Michigan, USA, for performing the tensile testing.

REFERENCES

[1]A. N. Gent, P. B. Lindley, and A. G. Thomas, *J. Appl. Polym. Sci.* **8**, 455 (1964).

[2]M. D. Ellul, "Mechanical Fatigue," in *Engineering with Rubber—How to Design Rubber Components*, 3rd ed., A. N. Gent, Ed., Carl Hanser Verlag, Munich, 2010.

[3]W. V. Mars, RUBBER CHEM. TECHNOL. **80**, 481 (2007).

[4]I. Masquelier, "Influence de la formulation sur les propriétés en fatigue d'élastomères industriels," Ph.D. Dissertation, Brest, 2014.

[5]D. Penumadu, J.-C. Chin, S. Young, F. Ignatz-Hoover, T. Floyd, and P. Chapman, RUBBER CHEM. TECHNOL. **94**, 626 (2021).

[6]T. Glanowski, M. Le Saux, V. Le Saux, B. Huneau, C. Champy, P. Charrier, and Y. Marco, RUBBER CHEM. TECHNOL. **96**, 59 (2023).

[7]J. Kallungal, L. Chazeau, J.-M. Chenal, J. Adrien, E. Maire, C. Barrès, B. Cantaloube, and P. Heuillet, RUBBER CHEM. TECHNOL. **96**, 90 (2023).

[8]Li F., J. Liu, W. V. Mars, T. W. Chan, Y. Lu, H. Yang, and L. Zhang, *Int. J. Fatigue* **80**, 50 (2015).

[9]D. H. C. Wong, F. Ignatz-Hoover, A. Childress, G. L. Jackson, and A. Padmakumar, RUBBER CHEM. TECHNOL. **96**, 214 (2023).

[10]C. G. Robertson, L. B. Tunnicliffe, L. Maciag, M. A. Bauman, K. Miller, C. R. Herd, and W. V. Mars, *Polymers*, **12**, 203 (2020).

[11]ASTM Standard D1514, "Standard Test Method for Carbon Black—Sieve Residue," Annu. Book ASTM Stand. **09**.**01** (2020)

[12]H. W. Greensmith, *J. Polym. Sci.* **21**, 175 (1956).

[13]A. Kadir and A. G. Thomas, RUBBER CHEM. TECHNOL. **54**, 15 (1981).

[14]G. J. Lake, C. C. Lawrence, A. G. Thomas, RUBBER CHEM. TECHNOL. **73**, 801 (2000).

[15]K. Tsunoda, J. J. C. Busfield, K. L. Davies, and A. G. Thomas, *J. Mater. Sci.* **35**, 5187 (2000).

[16]A. N. Gent, RUBBER CHEM. Technol. **63**, 49 (1990).

[*Received March 2023, Revised October 2023*]